PHOTONICS Research

Free-space interferometer design for optical frequency dissemination and out-of-loop characterization below the 10^{-21}-level

Thomas Jürss, Gesine Grosche, and Sebastian Koke*

Physikalisch-Technische Bundesanstalt, 38116 Braunschweig, Germany
**Corresponding author: sebastian.koke@ptb.de*

Received 19 January 2023; revised 20 March 2023; accepted 19 April 2023; posted 21 April 2023 (Doc. ID 485899); published 1 June 2023

For improving the performance of optical frequency dissemination and the resolution of its out-of-loop (OOL) characterization, we investigate a compact free-space interferometer design in which a monolithic assembly forms the reference arm. Two interferometer designs are realized, and their environmental sensitivity is analyzed based on the properties of the materials involved. We elucidate that in these designs the temperature sensitivities of the out-of-loop signal paths are greater than for the reference arm. As the estimated temperature-variation-induced frequency transfer errors are observed to be the relevant limitation, the out-of-loop characterization signal can be regarded as a trustworthy upper limit of the frequency transfer error to a remote place. We demonstrate a fractional frequency transfer uncertainty and OOL characterization resolution of $\leq 2.7 \times 10^{-21}$ over many measurement runs. With a value of $(0.23 \pm 1.07) \times 10^{-22}$ the weighted mean offset is significantly below the best reported results so far.

https://doi.org/10.1364/PRJ.485899

1. INTRODUCTION

Accurate interferometry underpins many high-precision measurements ranging from, e.g., gravitational wave detection [1], over Earth rotation sensing [2] to volume determination of silicon spheres [3,4] for the revised SI kilogram [5]. In optical frequency transfer via interferometric fiber links (IFLs), accurate interferometry enables path length stabilization [6–9] achieving frequency transfer uncertainties at or below the 10^{-19} level over IFLs having a length >500 km [10–13]. Hence, IFLs are currently the only available means to remotely compare [14] the best optical clocks. These now reach systematic uncertainties below 3×10^{-18} [15–21]. Remote optical clock comparisons are not only considered as a prerequisite for a potential redefinition of the SI second [22,23] but also enable applications in chronometric leveling [15,20,24–26] or fundamental physics [27,28]. Despite the proven frequency transfer performance, the interferometric noise floor [8,9,29] was identified as limiting uncertainty contribution at averaging times ≥1000 s in recent assessments [12,13,30]. Further progress of IFL performance and study of remaining non-reciprocal effects [12,31] require an improved interferometer.

Uncompensated fiber paths, which are the source of interferometric noise, can be located either at the sender site or in the receiver at the remote end. A typical example at the sender end would be the (short) reference arm of the Michelson interferometer of which the IFL forms the long arm. At both the sender and the receiver ends, input and output fibers are often uncompensated. In remote clock comparisons [14,15,25,32], a single IFL is typically only one constituent in a longer frequency transfer chain [33]. In this case, it is sometimes possible to avoid uncompensated paths altogether, by ensuring that the input and output reference planes of successive IFLs coincide [34,35]. In practice, however, many setups, including commercially available equipment, still contain uncompensated paths. In some topologies, common-mode suppression between multiple uncompensated paths exposed to the same environment can be utilized to minimize the net interferometric noise contribution [36,37].

For assessing the frequency transfer performance—online in an optical clock comparison as well as for validating IFLs and their instrumentation, one typically implements an out-of-loop (OOL) characterization by looping back the light from the remote end to the sender and comparing the loop output signal to the input of the IFL. The OOL setup typically introduces additional interferometric noise, impacting the assessed frequency transfer uncertainty. Ideally, this OOL signal would characterize the complete frequency transfer error between the IFL sender input and receiver output. However, the loop

output signal typically bypasses part of the receiver setup and, therefore, this part of the frequency transfer error cannot be assessed. Worse, because the sender and the comparison setup reside at the same location, uncompensated paths are now exposed to the same environment and noise contributions may cancel, falsely suggesting a lower uncertainty than will be achieved for separated sender and receiver units. Nevertheless, the best one can do for a meaningful OOL characterization is to minimize uncompensated paths in the sender and comparison setup and avoid their mutual cancellation. Furthermore, it is important to ensure that different contributions do not mask each other, i.e., that the frequency transfer uncertainty assessed via the OOL signal is an upper limit to the frequency transfer error of the signal received at the remote end.

Here, we demonstrate a compact all-dielectric free-space interferometer, as an accurate yet easily implementable OOL characterization solution. Different from a recent implementation of a compact free-space interferometer [37], the central element is a monolithic assembly formed by optically contacting a polarizing beam splitter (PBS) with a quarter-wave plate (QWP) and a high-reflection (HR) mirror. We integrate this assembly into a compact OOL characterization setup and we report OOL fractional frequency uncertainties of 10^{-21} and below.

In the following section, we will elucidate the relevant principles of IFLs and introduce the terminology used throughout the paper. After that, we will continue with introducing and discussing our interferometer design in Section 3 and presenting the experimental results in Section 4. In Appendix A, we address strategies to further enhance the achieved performance in the future.

2. OPTICAL FREQUENCY DISSEMINATION

A. Interferometric Path Length Stabilization

Figure 1(a) shows the generic setup used for the fiber-based, stabilized frequency dissemination to a remote location depicted here as being implemented using fiber optics.

The path length stabilization relies on the retro-reflecting part of the light reaching the remote end back to the sender. In this way, the IFL forms one arm of an unbalanced Michelson interferometer. The round-trip phase evolution of the long arm to the remote end is stabilized with respect to a short reference arm using a phase-locked loop (PLL) actuating an inline acousto-optic modulator (AOM). A second AOM near the remote end serves to discriminate light reflected at the remote end from spurious reflections and backscattering along the IFL. Within the locking bandwidth, the PLL establishes phase coherence between the reference arm retroreflector (place A) and the remote end B. If propagation is reciprocal, i.e., the phase evolution is equal in forward and backward propagation directions, stabilization of the round-trip phase offset implies phase stabilization of the one-way signal [8]. Suppression of the fiber connection phase noise is constrained by the so-called delay limit [8], leading to a dynamic residual frequency transfer error Δf_{ctrl}.

In the following derivation of a mathematical treatment of the OOL signal, we assume that the purpose of the IFL is to transfer the optical frequency ν_{C_1} of the light wave incident

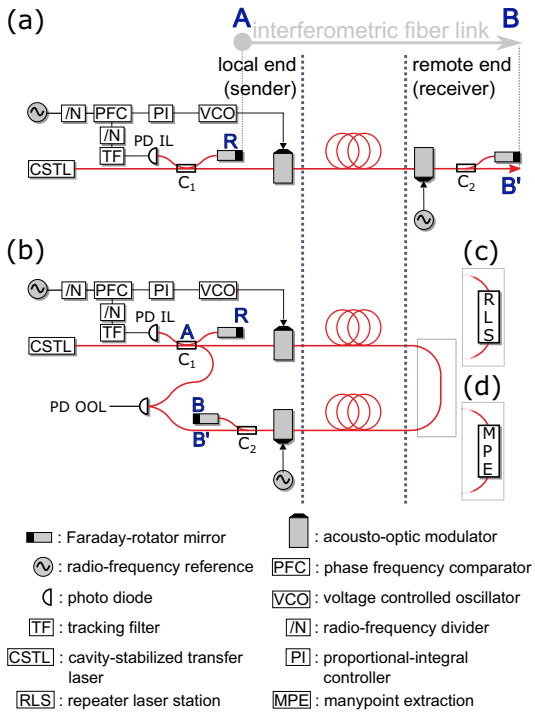

Fig. 1. (a) Generic setup of a long-distance IFL [7–9] transferring an optical frequency to a remote location. As an example, this setup is drawn based on fiber-optic interferometers and Faraday-rotator mirrors. The tracking filters are operated with a bandwidth higher than the propagation-delay-induced stabilization bandwidth [8] and radio-frequency dividers are used for achieving unambiguous phase resolution. (b) Loop-back setup for implementing an OOL characterization via heterodyning the IFL input with the loop output. In applications, one can use (c) a repeater laser station (RLS) [11] or (d) a manypoint extraction (MPE) [38] for tapping off a stabilized optical frequency at the remote end and for simultaneous IFL performance assessment using the loop-back.

from an ultrastable laser to the coupler C_1 to the remote place B'. This choice of the coupler C_1 as starting point simplifies the following argumentation since it is the splitting point between the long-haul fiber and reference arm. The treatment can easily be adapted to different choices of the starting point. Note that in some applications it is only required to achieve phase coherence between two locations physically different from the IFL input.

As elucidated above, the phase stabilization acts with respect to the short reference arm of the Michelson interferometer. Since this reference arm is not free of variations, the IFL essentially does not transfer the frequency ν_{C_1} but the frequency

$$\nu_A = \nu_{C_1} + \Delta f_{C_1\text{-}R\text{-}C_1}/2, \tag{1}$$

with $\Delta f_{C_1\text{-}R\text{-}C_1}$ being the frequency error introduced by the reference arm. The factor $1/2$ stems from the action of an idealized control loop within the stabilization bandwidth. For short, we will call this frequency error $\Delta f_{C_1\text{-}R\text{-}C_1}/2$ the in-loop (IL) contribution to the interferometric noise. Here and below, we make use of the definition of the frequency shift introduced by propagating from X to Y with

$$\Delta f_{X\text{-}Y}(t) = \frac{\mathrm{d}}{\mathrm{d}t}\int_0^{L_{XY}} \delta\phi(z, t - (\tau_{XY} - z/c_n))\mathrm{d}z, \quad (2)$$

where c_n is the speed of light in the fiber, L_{XY} is the geometric path length between the points X and Y, $\tau_{XY} = (z_Y - z_X)/c_n$ is the corresponding propagation delay, and $\delta\phi$ is the phase noise along the considered fiber path. We omit temporal variations of L_{XY} and τ_{XY} for the sake of simplicity. Furthermore, we introduce a short-cut notation for a concatenated path:

$$\Delta f_{X\text{-}Y\text{-}Z}(t) = \Delta f_{X\text{-}Y}(t - \tau_{YZ}) + \Delta f_{Y\text{-}Z}(t). \quad (3)$$

Similarly, there is a frequency error introduced at the remote end which results from the differential phase variation between the point B, which is the mid-way point actually stabilized by the IFL, and the location B', where the transferred frequency signal is effectively used:

$$\Delta f_{B',B} = \Delta f_{C_2\text{-}B'} - \Delta f_{C_2\text{-}B}. \quad (4)$$

Hence, assuming reciprocal propagation, the frequency transfer error $\Delta f = \nu_{B'} - \nu_{C_1}$ in stabilized operation can be written as

$$\Delta f = \Delta f_{\mathrm{ctrl}} + [\Delta f_{C_1\text{-}R\text{-}C_1}/2]_{E_s} + [\Delta f_{B',B}]_{E_r}, \quad (5)$$

where $[\cdot]_{E_x}$ specifies the environment driving the interferometric noise terms (E_s is the sender site and E_r is the remote site). Relevant environment variables are those that change the specific optical path length, for example, temperature, (air) pressure, and humidity; see, e.g., Ref. [34] for a detailed discussion.

As Eq. (5) shows, an accurate one-way frequency transfer requires minimizing $\Delta f_{C_1\text{-}R\text{-}C_1}$ and matching the frequency disturbances on the paths C_2–B and C_2–B', i.e., to minimize $\Delta f_{B',B}$. The mutual cancellation of disturbances has been discussed in the context of improving many point frequency extractions [38] and repeater laser stations [29]. In fiber optics this can be achieved by length matching the fiber leads after the fiber coupler and routing them close to each other in effectively the same environment [9,29,30,38]. Alternatively, the contribution C_2–B can be completely avoided by using a partial retro-reflector [7]. This is optimally placed at the user output B' to remove the C_2–B' contribution. A partial reflector can also be used at the sender instead of C_1 and R; however, this leads to unwanted multiple reflections into the link which can cause trouble, especially with amplifiers that amplify true and spurious signals equally.

B. Out-of-Loop Characterization

The loop-back configuration used for the OOL characterization of the IFL performance is shown in Fig. 1(b). While for the pure assessment of the IFL performance or its instrumentation a direct loop-back is often used, applications require to tap off the signal at the remote end, e.g., via a repeater laser station [11,29] [Fig. 1(c)] or a manypoint extraction [38] [Fig. 1(d)]. Uncompensated paths between the tapping point on the IFL and the effective user output are not monitorable by looping back and need to be taken into account in the construction and design phase of the extraction setups [11,29,38]. Here, we focus on the OOL signal and characterization of the contributions of sender-side imperfections on the basis of the setup shown in Fig. 1(b).

The observed frequency error in this OOL characterization in stabilized operation can be written as

$$\begin{aligned}\Delta f_{\mathrm{OOL}} &= \Delta f_{\mathrm{ctrl}} + [\Delta f_{C_1\text{-}R\text{-}C_1}/2 + \Delta f_{B',B} + \Delta f_{B'\text{-}C_1}]_{E_s} \\ &= \Delta f_{\mathrm{ctrl}} + [\Delta f_{C_1\text{-}R\text{-}C_1}/2 - \Delta f_{C_2\text{-}B} + \Delta f_{\mathrm{conn}}]_{E_s},\end{aligned} \quad (6)$$

with the optical path length variations of the connection used to generate the OOL beat being $\Delta f_{\mathrm{conn}} = \Delta f_{C_2\text{-}C_1}$.

Equation (6) shows that an additional contribution $\Delta f_{B'\text{-}C_1}$ limits the resolution of the OOL characterization. Furthermore, the rewrite in the last line of Eq. (6) points to an unwanted artifact in IFL OOL characterizations: common mode cancellations of the three terms $\Delta f_{C_1\text{-}R\text{-}C_1}/2$, $\Delta f_{C_2\text{-}B}$, and Δf_{conn} can arise from being immersed in effectively the same environment E_s. While such a common mode rejection is beneficial for a more stringent assessment of Δf_{ctrl} [9], it limits the significance of the OOL characterization as a measure of the frequency transfer uncertainty to remote locations since the fluctuations $\Delta f_{C_1\text{-}R\text{-}C_1}/2$ impacting the one-way frequency transfer are not completely visible in the OOL signal.

The impact of the Δf_{conn} contribution to the OOL signal can be avoided by implementing a two-way comparison between the loop output and the input [39,40], which typically requires an additional AOM in the setup shown in Fig. 1(b). However, even for a two-way comparison, the two uncompensated paths between the coupler and retro-reflector at both sides remain as interferometric uncertainty contributions. Here, we discuss a different strategy for enhancing the OOL resolution limit based on minimizing the environmental sensitivity of $\Delta f_{C_1\text{-}R\text{-}C_1}/2$ and Δf_{conn} together with rendering $\Delta f_{C_2\text{-}B} = 0$ by inline retro-reflection. This setup makes use of passive optical components only and does not require any two-way post-processing.

C. Assessment of the Interferometric Noise Floor

The interferometric noise floor is assessed by short-cutting the IFL rendering Δf_{ctrl} negligible:

$$\Delta f_{\mathrm{OOL,sc}} \simeq [\Delta f_{C_1\text{-}R\text{-}C_1}/2 - \Delta f_{C_2\text{-}B} + \Delta f_{\mathrm{conn}}]_{E_s}, \quad (7)$$

which defines the baseline for the OOL characterization signal from Eq. (6). The interferometric noise floor depends, as discussed above, on implementation details. These are not always described in publications or even known to the full extent rendering the comparison of results from different groups intricate. Table 1 summarizes published interferometric noise floor results together with the details mentioned. Reported fractional frequency instabilities of the interferometric noise floor are compared in Fig. 2.

Short-cutting the IFL not only removes the delay-limited phase noise contribution of the long-haul IFL but also changes the transfer function of the control path [8,42]. Hence, phase noise suppression features are different between short-cut configuration and long-haul IFL. Furthermore, other quantities such as the polarization variation dynamics may vary resulting in different frequency error contributions [8,43]. These effects need to be considered separately.

Table 1. Summary of Literature Interferometric Noise Floor Results Together with Disclosed Configuration Details and a Qualitative Classification[a]

Ref.	Configuration	IFL length	T stabilization	Estimated correlation $\Delta f_{C_1\text{-}R\text{-}C_1}/2$, $\Delta f_{C_2\text{-}B}$, and Δf_{conn}	Estimated magnitude Δf_{conn}	Type of counting & ADEV	Accuracy interferometric noise floor ($\times 10^{-21}$)
[8]	Free-space on Al breadboard	76 km	Passive	Partial	Large		
[9]	Fiber, optimized for $\Delta f_{\text{OOL,sc}} \simeq 0$ exploiting correlations of $\Delta f_{C_1\text{-}R\text{-}C_1}$, $\Delta f_{C_2\text{-}B}$, and Δf_{conn}	Short-cut	Passive	Partial–high	Low–moderate	Π, ADEV	3.5
[12]	Fiber, IL, and remote reference arm separately two-layer T shielded (inside Al housing in wooden box), same building/climatization as in Ref. [9]	Short-cut	Passive	Partial	Moderate–large	Λ, modADEV	–
[30]	Fiber, IL, and remote reference arm and connection in same housing	43 km	Passive	High	Low	Λ, modADEV	4.4 ± 2.3
[41]	Fiber, IL, and remote reference arm and connection in same T stabilized housing	Short-cut	Active	High	Low	Λ, modADEV	–
[36]	Multi-branch distribution, compact planar light wave circuit, two-branch difference	Short-cut	Passive	High	Low	modADEV	–
[37]	Multi-branch distribution, compact free-space, two-branch difference	Short-cut	Passive	Partial	Low	Λ, modADEV	–

[a]The corresponding published instabilities are depicted in Fig. 2.

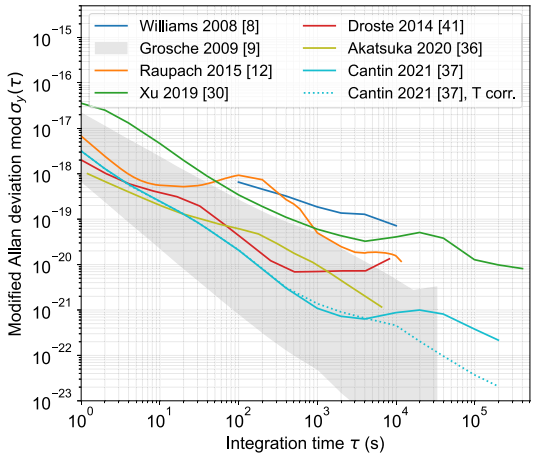

Fig. 2. Published state-of-the-art interferometric noise floor instabilities. The Π-counted ADEV results from Ref. [9] are indicated as possible Λ-counted modADEV range assuming white-phase noise domination on short time scales.

3. MONOLITHIC INTERFEROMETER

Our approach to simultaneously minimize the interferometer-induced contributions to frequency transfer uncertainty and OOL characterization uncertainty is illustrated in Fig. 3. We use a compact, free-space, all-dielectric interferometer layout. The central unit for path length stabilization is a monolithic assembly consisting of three optically contacted elements (manufactured by Layertec GmbH): a PBS made from fused silica and having an edge length of 10 mm, a low-order QWP made from a single quartz substrate (thickness 227 μm), and an HR mirror.

The rationale behind choosing optical contacting as the joining method instead of gluing is to avoid long-term creep of adhesives and their greater sensitivity toward changes in the environment.

The source light incident on the PBS is split up in its polarization components. The s-polarized portion is directed to the HR mirror and returns back to the PBS reflection plane p-polarized due to the action of the QWP. This path forms the reference arm of the Michelson interferometer. The p-polarized part of the incident light is transmitted through the PBS and focused into a single-mode IFL fiber, where it passes through a Faraday rotator (FR), two AOMs, and a polarization controller. At the far end of the IFL, the light beam hits a partially reflecting (PR) mirror terminating the IFL [7,30]. The polarization of the wave transmitted through the PR mirror is set to be linear. By doing so, the retro-reflected light propagates the fiber section backwards and due to 90° net polarization rotation by the FR double passage it is reflected by the PBS. The 90° net polarization rotation could also have been implemented using a QWP. After polarization projection, the beating with the

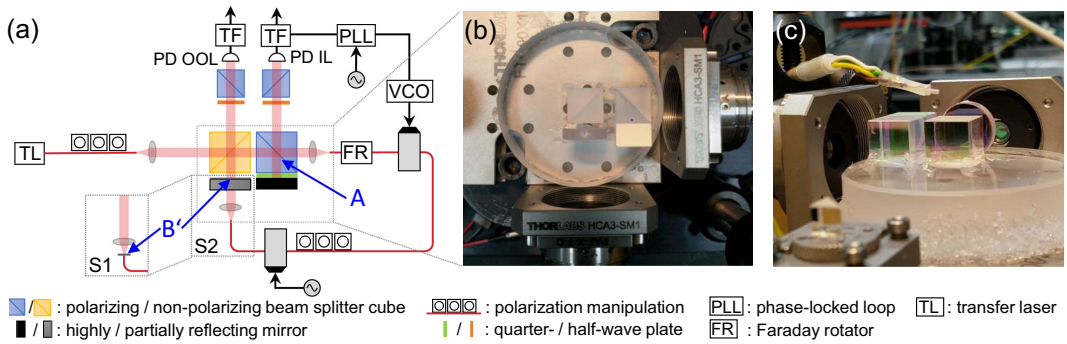

Fig. 3. (a) Schematic setup for the OOL characterization of the optical frequency dissemination performance of the monolithic interferometer design. The fibers have been taped down to the optical table. In the case of S1 and S2 using single-mode fibers on the IFL, the polarization at the far end has been set to linear horizontal polarization in front of the retro-reflector. For the S2PM configuration, all fibers and components have been exchanged for polarization-maintaining variants. For the measurements, the free-space part of the setup has been covered with a cardboard box together with the photodiodes. (b) Top view of the assembled configuration showing the monolithic assembly, the non-polarizing beam splitter, the fused silica baseplate, and the fiber bench with fiber collimators. (c) Side view of the assembled configuration showing the position of the calibrated PT100 temperature sensor.

reference arm light is recorded using a free-space photodiode. For the OOL characterization, the IFL output light is transmitted through the PR mirror and is superposed with a fraction of the input light beam tapped off by a non-polarizing beam splitter (NBS). Initially, we tried to optically contact the externally sourced monolithic IL assembly, the NBS, and the PR mirror to each other. Unfortunately, the achieved optical alignment was not sufficient so that in the following we kept the NBS and the retro-reflector separate and aligned them individually. The NBS is made from N-BK7, has an edge length of 10 mm, and is placed at a distance of approximately 3 mm to the monolithic assembly. Again, the beating is recorded after polarization projection with a free-space photodiode.

In order to avoid metallic optics mounts [8] with their larger thermal expansion, the monolithic assembly and the NBS are glued onto a fused silica substrate (diameter 50 mm, thickness 10 mm) by placing a fillet made from room temperature vulcanizing silicone at the free edges of the contact area between the beam splitter and substrate. This gluing procedure is inspired by other applications requiring a stress-less fixation of optical elements [44,45]. In the same manner, the substrate is glued onto an optical bench (Thorlabs, FT-100X100) used for fiber coupling.

We decided to base our setup upon beam splitter cubes for their standard availability and their ease in assembling the setup on commercially available fiber benches. The surfaces of these beam splitter cubes are anti-reflection coated in order to minimize potential etalon effects.

Two different positions of the PR retro-reflector have been realized. In a first version abbreviated as S1, we used an inline retro-reflector coated onto the fiber end resulting in a spatial separation of ≈37 mm between the PR mirror and NBS edge, i.e., a large OOL path length. Later we used an uncoated fiber and glued a PR mirror at a distance of ≈1.5 mm to the NBS edge using a UV curable epoxy (Optocast 3410 Gen2). This configuration has been characterized by an IFL consisting of single-mode fibers—in the following named S2, as well as using polarization-maintaining fibers for the IFL—identified as S2PM in the remainder.

The setup was placed on an optical table in a climatized laboratory. The servo and marker AOM drive frequencies have been −55 MHz and 40 MHz, respectively, for the S1 and S2 configurations resulting in IL and OLL beat frequencies of ≈30 MHz and ≈15 MHz. In the S2PM the IL and OOL beat frequencies have been lowered to ≈12 MHz and 6 MHz, respectively, using polarization-maintaining AOMs with drive frequencies of −74 MHz and 69 MHz. The fiber length of the characterization IFL in both setups has been <5 m, giving a negligible self-heterodyne phase noise contribution [8] induced by the phase noise of the narrow-linewidth fiber laser source with an operating wavelength of ≈1542 nm. The photodiode signals have been recorded with dead-time free counters (K+K FXE), which have been set to report 1 s phase averages of the frequency readings collected at the internal gate time of 1 ms. This type of phase averaging is also called Λ-averaging [46,47].

In the configurations S1 and S2, the polarization was manually optimized before the measurements. The following characterization concentrates on the configuration S2PM, as this avoids polarization effects to enter the assessment of the interferometric path length noise characterization. We assume that a performance similar to the characterization below can be achieved for non-polarization-maintaining fiber connections with stronger birefringence changes when using existing polarization stabilization techniques [48,49].

In this interferometer layout, the noise term $\Delta f_{C_1\text{-}R\text{-}C_1}$ in Eqs. (5) and (6) is given by the beam path between the PBS reflection plane and the HR mirror resulting in a geometric reference arm length of ≈2 × 5.2 mm for centric transversal. Furthermore, $\Delta f_{C_2\text{-}B} = \Delta f_{B',B} = 0$ due to inline retro-reflection. Accordingly, in our setup Δf_{conn} is induced by the optical path between the inline retro-reflector and the PBS reflection plane: $\Delta f_{\text{conn}} = \Delta f_{B'\text{-}C_1}$. In the following paragraph, we will quantify the temperature and air pressure sensitivities based on the properties of the involved materials.

A. Environmental Sensitivity Based on Material Properties

Variations in environmental variables χ induce a fractional frequency error given by [29,34]

Table 2. Materials Properties Used for the Calculation of the Environmental Sensitivities (Operating Conditions: $\lambda = 1542$ nm, $T = 20°C$, $p = 1004.04$ hPa, 0% Relative Humidity, 450 ppm CO_2 Concentration)[a]

Material	Element	n	$\partial n/\partial T$ [10^{-6} K^{-1}]	α [10^{-6} K^{-1}]	$\partial n/\partial p$ [10^{-9} hPa^{-1}]	κ [10^7 hPa]
N-BK7 [50]	NBS	1.50075	0.85310	7.10	≈1.76 [51]	46.5
Corning 7980 [52]	PBS	1.44408	9.4893	0.52	≈1.76 [51]	35.9
UV fused silica [53]	Base			0.55		37.2
Quartz [54]	$\lambda/4$	1.52778 (o) 1.53629 (e)	−5.6 (o) −6.7 (e)	12.4	1.03 (o) 1.075 (e)	≈38.3 at 589 nm
Stainless steel	Bench			10		160
Air [55,56]		1.00027	−0.91049		265.19	

[a]$\alpha = L^{-1} \times \partial L/\partial T$ is the coefficient of thermal expansion and κ is the bulk modulus.

Table 3. Environmental Sensitivity γ_χ of different Paths at Operation Wavelength $\lambda = 1542$ nm

Quantity	Path	γ_T [fs/K]	γ_p [as/hPa]
$\Delta f_{C_1\text{-}R\text{-}C_1}/2$	PBS–HR–PBS	0.18	≈0.01
Δf^{S1}_{conn}	PBS–NBS–fiber end	1.68	31.85
Δf^{S2}_{conn}	PBS–NBS–PR	0.33	3.98

$$y(t) = \frac{1}{c_0}\sum_i \left(\frac{\partial n_i}{\partial \chi_i} L_i + n_i \frac{\partial L_i}{\partial \chi_i}\right)\frac{\mathrm{d}\chi_i(t)}{\mathrm{d}t} = \sum_i \gamma_{\chi_i}\frac{\mathrm{d}\chi_i(t)}{\mathrm{d}t}, \quad (8)$$

where the summation takes into account different sections i of the considered optical paths with the refractive index n_i and geometrical length L_i, where c_0 is the speed of light in vacuum. As quantities χ_i, we will analyze and measure the impact of temperature (T) and air pressure (p) variations in the following. We will assume equilibrated environmental variations in the interferometric setup $\chi_i(t) = \chi(t)$ which we consider justified due to the compactness and the shielding of the setup.

Using Eq. (8) and the material properties listed in Table 2, we calculated the environmental sensitivities $\gamma_\chi = \sum_i \gamma_{\chi_i}$ of the different paths listed in Table 3. In calculating these sensitivities, we assumed centric transversal of the optics and modeled variations of the geometric lengths to act on the center-to-center distances. Furthermore, for describing the action of the QWP, we used the mean of ordinary and extraordinary refractive indices, the thermo-optic coefficient, and the pressure dependence of the refractive index. The impacts of air paths are described using an updated version [55] of the Edlén formula [57,58] and their partial derivatives with respect to T and p. We evaluate these at the working point derived from the barometric formula for a height of $h = 77$ m, a gravity constant $g = 9.81$ m s^{-2}, in standard atmosphere defined by the international civil aviation organization [air density $\rho_0 = 1.225$ kg/m^3, air pressure $p_0 = 1013.25$ hPa, relative humidity 0%, CO_2 concentration 450 ppm (parts per million)], giving $p = 1004.04$ hPa, and at the laboratory temperature of $T = 20°C$. For the configurations S2 and S2PM, we calculate [55,56] a sensitivity of −0.13 as/% relative humidity variation and we will see below that the resulting effects are negligible compared to the impact of T and p fluctuations.

The T and p sensitivities effective in OOL characterizations are obtained by adding the $\Delta f_{C_1\text{-}R\text{-}C_1}$ and Δf_{conn} sensitivities in the respective configurations yielding

$$\gamma^{S1}_{T,OOL} = 1.86 \text{ fs/K}, \qquad \gamma^{S1}_{p,OOL} \approx 31.86 \text{ as/hPa}, \quad (9)$$

$$\gamma^{S2}_{T,OOL} = 0.51 \text{ fs/K}, \qquad \gamma^{S2}_{p,OOL} \approx 4.00 \text{ as/hPa}. \quad (10)$$

As the sensitivities of the individual paths given in Table 3 show, the impact of T and p variations, considered separately, will only add up for the different paths. Hence, the OOL characterization signal overestimates the frequency error of the signal extracted at the remote end for pure T or pure p variations. A spurious mutual cancellation of noise terms in the OOL characterization is only possible by the combined impact of T and p variations. We will see below, however, that for the improved configuration S2 and for the interesting averaging times where the OOL signal starts to flicker, the typical estimated impact of T dominates over p up to averaging times of $\approx 3 \times 10^4$ s. Table 3 also shows that the p sensitivity mainly results from air paths of the free-space setup. By comparison, the single-mode fiber Corning SMF28 exhibits a temperature sensitivity of 37 fs/(K m) [29]. This shows that the IL and OOL T sensitivities are equivalent to uncompensated fiber paths of only 0.5 cm and 1.4 cm in length, respectively.

4. EXPERIMENTAL ASSESSMENT

Figure 4 compares the instabilities in the different configurations to the impact of T and p variations estimated on the basis of Eqs. (9) and (10) and simultaneous T and p measurements. Figure 4(a) for the S1 configuration shows that for averaging times >1000 s the observed OOL instabilities (red) match the estimated impact of T (green) and p (blue) variations well. In this configuration, we observe a crossover between being T variations limited, for averaging times between 10^3 s and 10^4 s, and being p variations limited for averaging times $\gtrsim 10^4$ s that is reflected in the OOL instability. From this finding and the close match between the measured and estimated temporal OOL phase evolution shown in Fig. 5, we deduce that the modeling of the environmental sensitivities approximates the reality to a high degree. The residual impact of T and p variations leads to a stagnation of the observed OOL fractional frequency instability at a level of $\approx 4 \times 10^{-21}$ in the S1 configuration.

For the configurations S2 and S2PM, however, the impact of p variations is greatly reduced due to the shortening of the air path between the retro-reflecting mirror and the NBS. For these configurations we observe OOL fractional frequency instabilities below 10^{-21} for averaging times above 5×10^4 s. For the S2PM configuration, we have achieved a significantly reduced short-term instability at averaging times <100 s.

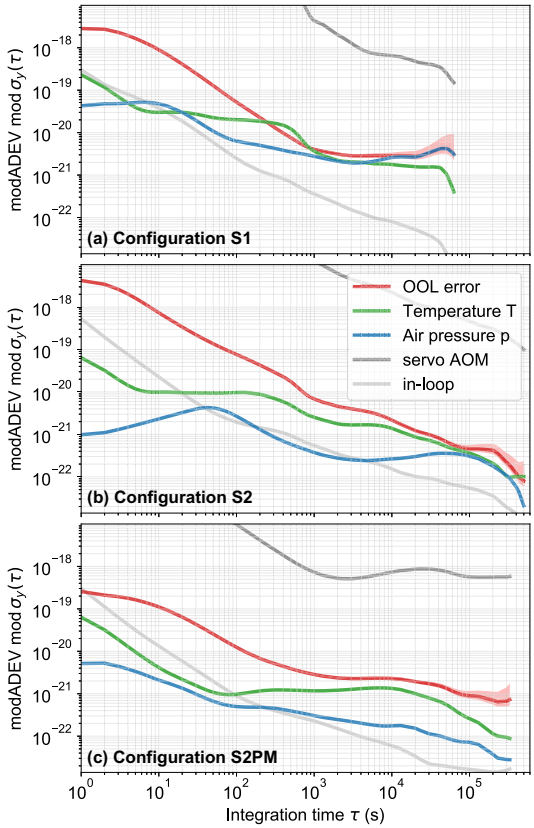

Fig. 4. Comparison of the instability of the OOL signal (red) to the estimated contributions of T variations (green) and p variations (blue) of the longest measurement runs in each of the three configurations. Temperature variations have been measured using a PT100 T probe close to the monolithic assembly as shown in Fig. 3(c). The light and dark gray curves display the instabilities of the IL signal and the servo AOM drive frequency, respectively. The latter can be interpreted as the frequency instability of the fiber connections. Air pressure data in (a) and (c) stem from a barometer placed in a neighboring laboratory in the same building at PTB. In (b), due to unavailability of data from the PTB barometer, air pressure data from the climate station of the Department of Hydrology and River Basin Management of Technical University Braunschweig have been used, which is ≈6 km apart. At times of overlapping operation, we have observed matching p instabilities of both barometers for averaging times $\tau > 1000$ s. This shows that the exact placement of the barometer is of minor importance for the assessment of the potential impact of p in the OOL characterization.

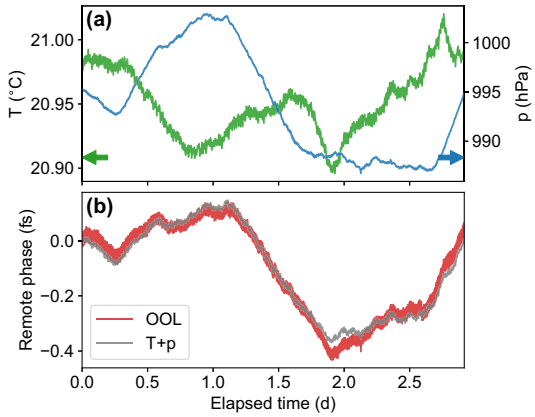

Fig. 5. (a) As an example, typical T and p variations in our lab. The data are the same as underlying Fig. 4(a). (b) Together with the T and p sensitivities from Eq. (9) one observes a close match of the measured OOL phase evolution with the estimated one for the S1 configuration.

While switching from the S2 to the S2PM configuration, we observed that this reduction mainly resulted from using a PM fiber connection between the source laser and the entrance of the interferometer setup. An additional improvement of the short-term instability below averaging times of 4 s has been achieved by enhancing the signal-to-noise ratio of the beats. The S2 and S2PM measurements also show a larger discrepancy from the estimates of the impact of T and p variations than the S1 measurement. This is observable in the instabilities in Figs. 4(b) and 4(c) and also in the time traces (not shown), which hints to uncharacterized OOL processes not described by the material response (see discussion below).

In the S2PM configuration we have performed several measurement runs to analyze the statistics of its performance. Figure 6(a) shows the observed instabilities and compares these to the results of Akatsuka *et al.* [36], Cantin *et al.* [37], and to the instability contribution of the stabilization electronics. The instability of the OOL signal displays a reproducible behavior for averaging times <100 s, with a spread in the results below a factor of 2. Measurements with shorter gate time (not displayed) show a modADEV progression proportional to $\tau^{-3/2}$ for averaging times between 10^{-3} s and 10^{-1} s and a shoulder-like contribution setting in around 1 s in configuration S2PM (≈0.5 s for configuration S2). The OOL phase noise density in Fig. 6(b) (Symmetricom 5125A) shows that the latter contribution results from a steep phase noise increase below 1 Hz. We checked that neither the tracking filters [orange trace in Fig. 6(b)] nor the combination of analog phase-frequency comparator and proportional-integral controller [gray trace in Fig. 6(b)] is responsible for this phase noise contribution.

For longer averaging times, the OOL instabilities in Fig. 6(a) again exhibit a stagnation at a level understandable by the T variations (green curves). In the future, an improved passive and active T stabilization may enhance the results in this range. For averaging times between 10^3 s and 5×10^4 s, the estimated p-induced instabilities (blue curves) are approximately a factor of 10 below. This shows that a mutual complete cancellation of T and p is not present in these measurements.

The OOL instabilities we obtain are up to averaging times of 200 s below the best reported interferometric OOL characterization noise floors so far. For longer averaging times, only the interferometric noise floor of the multi-branch frequency distribution systems [36,37] shows comparable low instabilities: while the result of Akatsuka *et al.* [36] shows an instability at the lower edge of the range we observe, the result of Cantin *et al.* [37] levels off due to T variations a factor of ≈5 below our average performance. Both results, however, are essentially the inter-branch comparison of compact interferometric ensembles designed to maximize the inter-branch common-mode noise rejection [36,37] and, hence, quantify the uncertainty of the multi-branch frequency distributions system. When a pair of

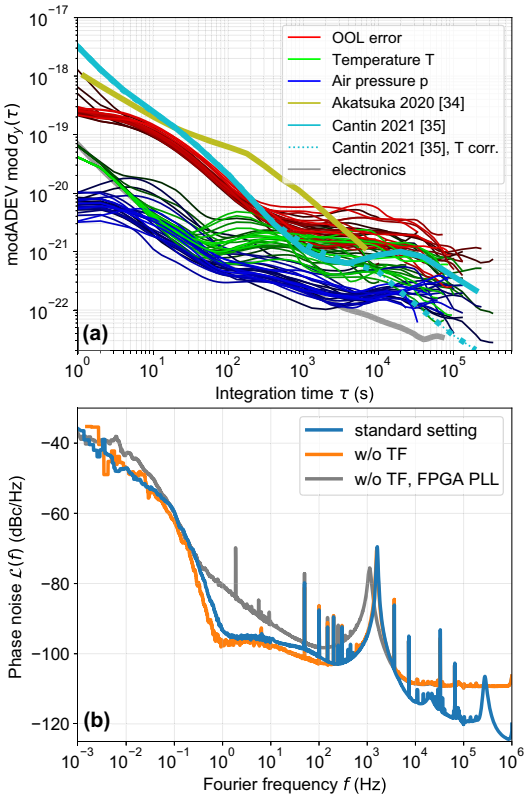

Fig. 6. (a) Observed instability of the OOL signal (red curves with varying shade) and of the estimated T (green curves with varying shade) and p (blue curves with varying shade) variations for multiple runs in the S2PM configuration. For comparison the instabilities published by Akatsuka *et al.* [36] and Cantin *et al.* [37] are included. The gray line shows the instability of the IL signal when the PD signal is replaced by an electronic signal. (b) Typical OOL phase noise densities for configuration S2PM and for modified setups without using tracking filters (TFs) and using a field-programmable gated array-based PLL [59]. The prominent phase noise peaks around 1 kHz are the servo bumps of the IFL stabilization. The lower phase noise reduction achieved for the blue trace compared to the orange between 10 kHz and 1 MHz is due to the tracking filter. The phase noise feature in the blue curve at ≈300 kHz is the servo bump of the tracking filter PLL.

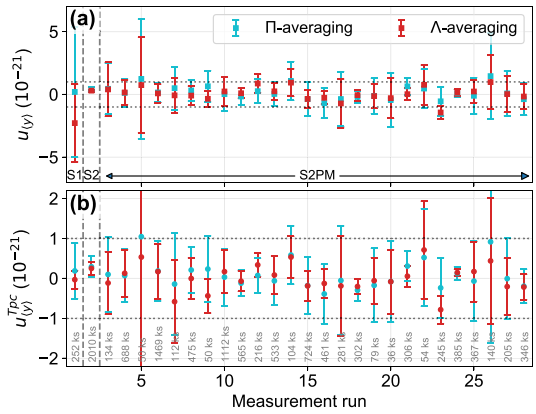

Fig. 7. (a) Π and Λ-averaged OOL frequency offsets over the different measurement runs. The statistical uncertainty of the offsets is estimated by the overlapping ADEV and modADEV, respectively, at an averaging time of $\tau = T_d/4$ (T_d, duration of the measurement run). (b) Residuals of the OOL frequency offsets after accounting for the estimated phase contribution of the measured T and p variations. The light and dark gray curves display the instabilities of the IL stabilization and the servo AOM drive frequency, respectively. The latter can be regarded as the free-running fiber noise of the IFL fibers.

those branches are used for dissemination and OOL characterization, this inter-branch comparison signal does not necessarily quantify the frequency transfer error to a remote place at the same uncertainty level due to common-mode rejection. Interestingly, the instability Cantin *et al.* [37] report after compensating for the measured T variations falls significantly below the estimated impact of p variation on our 4.5 mm long OOL air path. Assuming a similarly long air path of the interferometric ensemble and expecting long-term p variations to be comparable in Paris and Braunschweig, this also indicates a high degree of common-mode rejection.

Figure 7 shows the OOL fractional frequency transfer uncertainties in several measurement runs for Π and Λ averaging. For 25 out of the 28 measurement runs shown in Fig. 7(a), the observed fractional frequency uncertainties are below 2.7×10^{-21} with the offsets exceeding 1.0×10^{-21} in only three (Π-averaging) and two (Λ-averaging) cases (see dotted line). The observed OOL frequency offsets are also compatible with zero within 1σ (σ being the statistical uncertainty contribution) for 27 (Π-averaging) and 25 (Λ-averaging) out of the 28 measurement runs. The observed offsets are therefore roughly a factor of 4 better than previously published inaccuracies (see Table 1).

Figure 7(b) shows the residual uncertainties after compensating for the estimated impact of T and p variations. These residual uncertainties scatter on a lower level with 22 of the 28 runs being below 1.0×10^{-21} (Λ-averaging). The zero-compatibility is as distinct as for the analysis without T and p compensation. The $1/\sigma^2$-weighted average of all measurement runs in S2PM configuration is $(0.23 \pm 1.07) \times 10^{-22}$ and $(2.18 \pm 8.53) \times 10^{-23}$ for Π and Λ averaging, respectively. After compensating for the estimated impact of T and p variations, these weighted averages are $(1.37 \pm 8.60) \times 10^{-23}$ and $(1.08 \pm 6.99) \times 10^{-23}$, respectively. This shows, as the scattering of the individual runs, that the overall uncertainty is reduced by accounting for the T and p variations.

However, this reduction is not pronounced, which indicates that there are uncharacterized OOL processes with a similar magnitude present in our system. Free-space interferometers are susceptible to uncertainty contributions resulting from optics movements and related beam pointing variations. A full description of this effect requires integrating the electric field interference of the two heterodyned beams over the photodiode surface [60] including their spatial wavefronts. In our setup, the focal length of the fiber collimator used is 7.5 mm (Thorlabs, PAF-X-7-C) resulting in a collimated beam diameter of ≈1.4 mm for the 10.4 μm mode field diameter of the prototypical Corning SMF28 fiber. For such a collimation, the Rayleigh range is $z_R \approx 1.0$ m. Hence, we expect the wavefront curvature and the Gouy phase shift to play a lesser role and expect the geometrical contributions to be dominated by

mutual longitudinal shifts of the beams and angle effects. In the case where longitudinal shifts are assumed to be the only source of phase disturbances, the offsets we observe would correspond to ≤150 nm beam displacements, which does not seem to be out of range given the mounting of optics in our setup. Such residual OOL errors may also result from movements of the retro-reflecting mirror, e.g., by changes of the UV curable adhesive underneath. Indeed, a comparison of the observed temporal phase variations with the ones estimated by T and p variations (not shown) indicates that often the estimated T variations do not completely account for the observed OOL phase error and that on average a factor of ≈2.2 is required to minimize the discrepancy. Further studies have to show whether different adhesives or making the setup more compact by fixing the NBS, PBS, and miniaturized fiber couplers to the same baseplate leads to a reduction of such OOL processes.

A different OOL process may result from air humidity h variations in the air paths, which we have not addressed so far. By combining the above-mentioned relative humidity sensitivity of −0.13 as/% with the typical relative air humidity variation measurements in the same laboratory [34], we estimate the uncertainty contribution of these effects to be $\leq 5 \times 10^{-23}$ for averaging times between 10^3 s and 10^5 s. Hence, air humidity variations can be ruled out as the source of the observed discrepancy.

Furthermore, ghost beams as, e.g., discussed in the gravitational wave detection community [61–63] may contribute to the OOL signal. In our setup relevant ghost beams have to be polarized orthogonal to the outgoing signal. Hence, residual reflections of AR coatings in the linearly-polarized beam path are of lesser importance. However, there are two relevant ghost beam sources: first, backreflections or Rayleigh backscattering with orthogonal polarization in the path between the Faraday rotator and servo AOM. Rayleigh backscattering strength lies in the range of a few ppm per meter [62]. This may result in a ghost-beam-induced phase error $\phi_{\mathrm{err}} = a_{\mathrm{sp}}/a \sin \phi_{\mathrm{sp}}$ [62] (a, amplitude of the signal; a_{sp}, ϕ_{sp}, ghost beam amplitude and phase, respectively). The induced fractional frequency uncertainty contribution depends on the dynamics of the phase of the ghost beam. In the worst case of a π-rotation of ϕ_{sp} over the measurement time t, the uncertainty contribution is $\leq 5 \times 10^{-18}/(t/\mathrm{s})$. A similar calculation for the estimated 40 dB power return loss of the AOM gives an uncertainty estimate of $\leq 1.7 \times 10^{-17}/(t/\mathrm{s})$. The second ghost beam source is light that is transmitted through the PR mirror and that is then reflected by the NBS. This ghost beam can make a second round through the IFL leading to a beat at the same round-trip frequency as the IL beat. From the spurious beats in the measured signals, we estimate spurious signal contribution of at least 30 dB below the IL stabilization beat leading to an estimated uncertainty contribution of $\leq 5 \times 10^{-17}/(t/\mathrm{s})$. These estimations show that, for the typical duration of the continuous measurement runs of ≥50 ks, the estimated uncertainty contribution is on a relevant level of $\leq 1 \times 10^{-21}$. In the future, the ghost beam uncertainty contribution can be further minimized by using, e.g., a PBS instead of an NBS as the element tapping of input light for the OOL measurement.

Finally, the uncharacterized OOL processes may result from electronic contributions, e.g., via the temperature dependence of the components. We estimated the electronic noise contribution of the control loop by deriving a surrogate for the photodiode signal from a commonly referenced synthesizer and connecting the voltage-controlled oscillator (VCO) output to the OOL signal tracking filter input [see Fig. 3(a)]. The gray curve in Fig. 6(a) shows that the instability of this signal is more than 1 order of magnitude below the observed OOL signal instabilities. Hence, electronic components within this loop can be ruled out as a possible cause, so that only processes in the photodetectors remain as the possible origin.

5. CONCLUSIONS

We have presented a compact, free-space interferometer layout for OOL characterization that uses an optically contacted, monolithic assembly for the reference arm rendering it robust against external disturbances and misalignment. Using this interferometer layout, we improve the OOL characterization resolution in fiber-based frequency transfer to $\leq 2.7 \times 10^{-21}$. The temperature sensitivity of the OOL signal path is greater than that of the reference arm, so that the OOL signal quantifies the maximum remote place frequency transfer error induced by sender side temperature variations. Estimations of the impact of temperature and pressure variations based on the properties of the materials involved are close to the observed out-of-loop characterization signal variations. This opens up the possibility of post-correction for these error sources [30,37], while further studies have to elucidate the origin of the observed discrepancies below the 10^{-21} level.

In the current implementation the temperature sensitivity has been limiting for averaging times of 1000 s and longer. In the future, this constraint can be lowered further with refined layouts (see Appendix A) and active temperature stabilization.

We believe this research will stimulate further advances in lowering the uncertainty of optical frequency transfer and analysis of its fundamental limitations, and it will prove valuable for applications such as chronometric leveling between two non-laboratory sites.

APPENDIX A: STRATEGIES FOR FURTHER REDUCING THE ENVIRONMENTAL SENSITIVITY

In this appendix, we address how the system performance can be further improved in the future.

One strategy to minimize the external parameter sensitivity of the IL and OOL signals could be to use glasses with less T sensitivity γ_T/L of the optical path length, e.g., in an all-dielectric design by optically contacting the NBS and PR mirror to the monolithic assembly. Figure 8 shows the temperature sensitivities γ_T/L for different optical glasses from prominent glass manufacturers. The comparison with the temperature sensitivity $\gamma_{T,\mathrm{OOL}}^{(\mathrm{S2})}/L$ shows that there is no glass with bulk T sensitivity lower than the compound sensitivity of our interferometer in S2 configuration. Hence, in order to make progress beyond our results, the optics sizes have to be decreased in such an all-dielectric design. Future investigations have to show whether optical contacting of smaller optics is feasible.

A different strategy could be to render the whole system athermal combining different material properties. For instance,

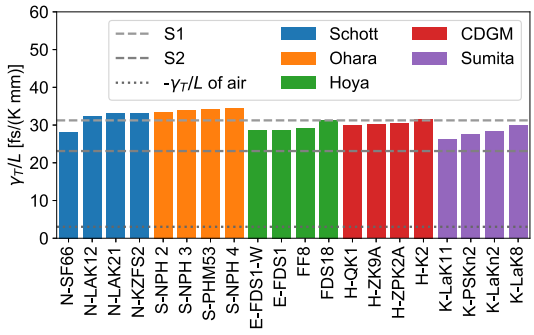

Fig. 8. Temperature sensitivities γ_T per optical path length L for different optical glasses from the vendors Schott, Ohara, Hoya, CDGM, and Sumita in comparison to $\gamma_{T,\mathrm{OOL}}^{(\mathrm{S1})}/L_{\mathrm{S1}}$, $\gamma_{T,\mathrm{OOL}}^{(\mathrm{S2})}/L_{\mathrm{S2}}$, and $\gamma_T^{(\mathrm{air})}/L_{\mathrm{air}}$. Shown are the four least temperature-sensitive glasses of each manufacturer. Considering all glasses listed in the respective catalogues, the values spread over a range from $\approx$26.5 fs K^{-1} mm^{-1} to $\approx$100 fs K^{-1} mm^{-1}.

this could be achieved using discrete optical elements attached to a common baseplate to engineer the baseplate materials such that its length change with temperature compensates for the negative temperature sensitivity $\gamma_T^{(\mathrm{air})}$ of the air paths.

We performed an analysis based on the assumption that the temperature-induced expansion of the two-dimensional baseplate is homogeneous. This analysis shows that well accessible materials such as fused silica variants like Corning 7980 listed in Table 2 or the Fe-36Ni metal alloy [64] match the relative T sensitivity of air quite well. Hence, it seems feasible that T sensitivities of $|\gamma_T^{(\mathrm{discrete})}|/L \leq 1.4$ fs K^{-1} mm^{-1}, i.e., more than an order of magnitude lower than for S2, can be reached.

The comparison with estimated impact of T and p variations in Fig. 4 shows that, for a factor of 10 lower T sensitivities, the p sensitivity is expected to become dominating. The impact of p variations can only be mitigated by evacuating the interferometer. While adding technical complexity, we estimate that another factor of 4 improvement to a T sensitivity of $|\gamma_T^{(\mathrm{evacuated})}|/L \leq 0.35$ fs K^{-1} mm^{-1} for an evacuated interferometer with discrete optics mounted on a baseplate made from an ultralow expansion glass or ceramics is viable.

Funding. Deutsche Forschungsgemeinschaft (CRC 1464 Terra-Q (Project-ID 434617780), EXC-2123 Quantum Frontiers (Project-ID 390837967)); European Metrology Programme for Innovation and Research (18SIB06 TiFOON).

Acknowledgment. We thank Alexandre Didier and Tanja Mehlstäubler for providing the UV curable adhesive, the group of Uwe Sterr and Tim Müller from the Department of Hydrology and River Basin Management of the Technical University Braunschweig for providing the air pressure measurements. We are grateful to Thomas Legero and Uwe Sterr for the PT100 temperature sensor calibration. We acknowledge fruitful discussions with Jochen Kronjäger, Erik Benkler, Alexander Kuhl, Thomas Waterholter, Andreas Koczwara (all PTB), Gudrun Wanner (AEI), Stephan Anders and Peter Zimmermann (both Layertec). The published work is part of the TiFOON project. This project has received funding from the EMPIR programme co-financed by the Participating States and from the European Union's Horizon 2020 research and innovation programme. In addition, we received funding from the Deutsche Forschungsgemeinschaft (DFG, German Research Foundation) under Germany's Excellence Strategy Quantum Frontiers.

Disclosures. The authors declare no conflicts of interest.

Data Availability. Data underlying the results presented in this paper are available at Ref. [65].

REFERENCES

1. B. Abbott, R. Abbott, and T. Abbott, LIGO Scientific Collaboration, and Virgo Collaboration, "Observation of gravitational waves from a binary black hole merger," Phys. Rev. Lett. **116**, 061102 (2016).
2. K. U. Schreiber and J.-P. R. Wells, "Invited review article: large ring lasers for rotation sensing," Rev. Sci. Instrum. **84**, 041101 (2013).
3. N. Kuramoto, K. Fujii, and K. Yamazawa, "Volume measurements of ^{28}Si spheres using an interferometer with a flat etalon to determine the Avogadro constant," Metrologia **48**, S83–S95 (2011).
4. A. Nicolaus, G. Bartl, A. Peter, E. Kuhn, and T. Mai, "Volume determination of two spheres of the new ^{28}Si crystal of PTB," Metrologia **54**, 512–515 (2017).
5. https://www.bipm.org/en/home.
6. L.-S. Ma, P. Jungner, J. Ye, and J. L. Hall, "Delivering the same optical frequency at two places: accurate cancellation of phase noise introduced by an optical fiber or other time-varying path," Opt. Lett. **19**, 1777–1779 (1994).
7. S. M. Foreman, K. W. Holman, D. D. Hudson, D. J. Jones, and J. Ye, "Remote transfer of ultrastable frequency references via fiber networks," Rev. Sci. Instrum. **78**, 021101 (2007).
8. P. A. Williams, W. C. Swann, and N. R. Newbury, "High-stability transfer of an optical frequency over long fiber-optic links," J. Opt. Soc. Am. B **25**, 1284–1293 (2008).
9. G. Grosche, O. Terra, K. Predehl, R. Holzwarth, B. Lipphardt, F. Vogt, U. Sterr, and H. Schnatz, "Optical frequency transfer via 146 km fiber link with 10^{-19} relative accuracy," Opt. Lett. **34**, 2270–2272 (2009).
10. D. Calonico, E. K. Bertacco, C. E. Calosso, C. Clivati, G. A. Costanzo, M. Frittelli, A. Godone, A. Mura, N. Poli, D. V. Sutyrin, G. Tino, M. E. Zucco, and F. Levi, "High-accuracy coherent optical frequency transfer over a doubled 642-km fiber link," Appl. Phys. B **117**, 979–986 (2014).
11. N. Chiodo, N. Quintin, F. Stefani, F. Wiotte, E. Camisard, C. Chardonnet, G. Santarelli, A. Amy-Klein, P.-E. Pottie, and O. Lopez, "Cascaded optical fiber link using the internet network for remote clocks comparison," Opt. Express **23**, 33927–33937 (2015).
12. S. M. F. Raupach, A. Koczwara, and G. Grosche, "Brillouin amplification supports 1×10^{-20} uncertainty in optical frequency transfer over 1400 km of underground fiber," Phys. Rev. A **92**, 021801 (2015).
13. S. Koke, A. Kuhl, T. Waterholter, S. M. F. Raupach, O. Lopez, E. Cantin, N. Quintin, A. Amy-Klein, P.-E. Pottie, and G. Grosche, "Combining fiber Brillouin amplification with a repeater laser station for fiber-based optical frequency dissemination over 1400 km," New J. Phys. **21**, 123017 (2019).
14. C. Lisdat, G. Grosche, N. Quintin, C. Shi, S. M. F. Raupach, C. Grebing, D. Nicolodi, F. Stefani, A. Al-Masoudi, S. Dörscher, S. Häfner, J.-L. Robyr, N. Chiodo, S. Bilicki, E. Bookjans, A. Koczwara, S. Koke, A. Kuhl, F. Wiotte, F. Meynadier, E. Camisard, M. Abgrall, M. Lours, T. Legero, H. Schnatz, U. Sterr, H. Denker, C. Chardonnet, Y. Le Coq, G. Santarelli, A. Amy-Klein, R. Le Targat, J. Lodewyck, O. Lopez, and P.-E. Pottie, "A clock network for Geodesy and fundamental science," Nat. Commun. **7**, 12443 (2016).

15. M. Takamoto, I. Ushijima, N. Ohmae, T. Yahagi, K. Kokado, H. Shinkai, and H. Katori, "Test of general relativity by a pair of transportable optical lattice clocks," Nat. Photonics **14**, 411–415 (2020).
16. C. W. Chou, D. B. Hume, T. Rosenband, and D. J. Wineland, "Optical clocks and relativity," Science **329**, 1630–1633 (2010).
17. I. Ushijima, M. Takamoto, M. Das, T. Ohkubo, and H. Katori, "Cryogenic optical lattice clocks," Nat. Photonics **9**, 185–189 (2015).
18. T. Nicholson, S. Campbell, R. Hutson, G. Marti, B. Bloom, R. McNally, W. Zhang, M. Barrett, M. Safronova, G. Strouse, W. Tew, and J. Ye, "Systematic evaluation of an atomic clock at 2×10^{-18} total uncertainty," Nat. Commun. **6**, 6896 (2015).
19. N. Huntemann, C. Sanner, B. Lipphardt, C. Tamm, and E. Peik, "Single-ion atomic clock with 3×10^{-18} systematic uncertainty," Phys. Rev. Lett. **116**, 063001 (2016).
20. W. F. McGrew, X. Zhang, R. J. Fasano, S. A. Schäffer, K. Beloy, D. Nicolodi, R. C. Brown, N. Hinkley, G. Milani, M. Schioppo, T. H. Yoon, and A. D. Ludlow, "Atomic clock performance enabling Geodesy below the centimetre level," Nature **564**, 87–90 (2018).
21. S. Brewer, J.-S. Chen, A. Hankin, E. Clements, C. Chou, D. Wineland, D. Hume, and D. Leibrandt, "$^{27}Al^{+}$ quantum-logic clock with a systematic uncertainty below 10^{-18}," Phys. Rev. Lett. **123**, 033201 (2019).
22. F. Riehle, "Towards a redefinition of the second based on optical atomic clocks," C. R. Phys. **16**, 506–515 (2015).
23. P. Gill, "Is the time right for a redefinition of the second by optical atomic clocks?" J. Phys. Conf. Ser. **723**, 012053 (2016).
24. T. Takano, M. Takamoto, I. Ushijima, N. Ohmae, T. Akatsuka, A. Yamaguchi, Y. Kuroishi, H. Munekane, B. Miyahara, and H. Katori, "Geopotential measurements with synchronously linked optical lattice clocks," Nat. Photonics **10**, 662–666 (2016).
25. J. Grotti, S. Koller, S. Vogt, S. Häfner, U. Sterr, C. Lisdat, H. Denker, C. Voigt, L. Timmen, A. Rolland, F. N. Baynes, H. S. Margolis, M. Zampaolo, P. Thoumany, M. Pizzocaro, B. Rauf, F. Bregolin, A. Tampellini, P. Barbieri, M. Zucco, G. A. Costanzo, C. Clivati, F. Levi, and D. Calonico, "Geodesy and metrology with a transportable optical clock," Nat. Phys. **14**, 437–441 (2018).
26. T. E. Mehlstäubler, G. Grosche, C. Lisdat, P. O. Schmidt, and H. Denker, "Atomic clocks for geodesy," Rep. Prog. Phys. **81**, 064401 (2018).
27. P. Delva, J. Lodewyck, S. Bilicki, E. Bookjans, G. Vallet, R. Le Targat, P.-E. Pottie, C. Guerlin, F. Meynadier, C. Le Poncin-Lafitte, O. Lopez, A. Amy-Klein, W.-K. Lee, N. Quintin, C. Lisdat, A. Al-Masoudi, S. Dörscher, C. Grebing, G. Grosche, A. Kuhl, S. Raupach, U. Sterr, I. R. Hill, R. Hobson, W. Bowden, J. Kronjäger, G. Marra, A. Rolland, F. N. Baynes, H. S. Margolis, and P. Gill, "Test of special relativity using a fiber network of optical clocks," Phys. Rev. Lett. **118**, 221102 (2017).
28. B. M. Roberts, P. Delva, A. Al-Masoudi, A. Amy-Klein, C. Bærentsen, C. F. A. Baynham, E. Benkler, S. Bilicki, S. Bize, W. Bowden, J. Calvert, V. Cambier, E. Cantin, E. A. Curtis, S. Dörscher, M. Favier, F. Frank, P. Gill, R. M. Godun, G. Grosche, C. Guo, A. Hees, I. R. Hill, R. Hobson, N. Huntemann, J. Kronjäger, S. Koke, A. Kuhl, R. Lange, T. Legero, B. Lipphardt, C. Lisdat, J. Lodewyck, O. Lopez, H. S. Margolis, H. Álvarez-Martínez, F. Meynadier, F. Ozimek, E. Peik, P.-E. Pottie, N. Quintin, C. Sanner, L. De Sarlo, M. Schioppo, R. Schwarz, A. Silva, U. Sterr, C. Tamm, R. Le Targat, P. Tuckey, G. Vallet, T. Waterholter, D. Xu, and P. Wolf, "Search for transient variations of the fine structure constant and dark matter using fiber-linked optical atomic clocks," New J. Phys. **22**, 093010 (2020).
29. F. Stefani, O. Lopez, A. Bercy, W.-K. Lee, C. Chardonnet, G. Santarelli, P.-E. Pottie, and A. Amy-Klein, "Tackling the limits of optical fiber links," J. Opt. Soc. Am. B **32**, 787–797 (2015).
30. D. Xu, P. Delva, O. Lopez, A. Amy-Klein, and P.-E. Pottie, "Reciprocity of propagation in optical fiber links demonstrated to 10^{-21}," Opt. Express **27**, 36965–36975 (2019).
31. D. Xu, O. Lopez, A. Amy-Klein, and P.-E. Pottie, "Non-reciprocity in optical fiber links: experimental evidence," Opt. Express **29**, 17476–17490 (2021).
32. J. Guéna, S. Weyers, M. Abgrall, C. Grebing, V. Gerginov, P. Rosenbusch, S. Bize, B. Lipphardt, H. Denker, N. Quintin, S. M. F. Raupach, D. Nicolodi, F. Stefani, N. Chiodo, S. Koke, A. Kuhl, F. Wiotte, F. Meynadier, E. Camisard, C. Chardonnet, Y. Le Coq, M. Lours, G. Santarelli, A. Amy-Klein, R. Le Targat, O. Lopez, P. E. Pottie, and G. Grosche, "First international comparison of fountain primary frequency standards via a long distance optical fiber link," Metrologia **54**, 348–354 (2017).
33. J. Lodewyck, R. Le Targat, P.-E. Pottie, E. Benkler, S. Koke, and J. Kronjäger, "Universal formalism for data sharing and processing in clock comparison networks," Phys. Rev. Res. **2**, 043269 (2020).
34. E. Benkler, B. Lipphardt, T. Puppe, R. Wilk, F. Rohde, and U. Sterr, "End-to-end topology for fiber comb based optical frequency transfer at the 10^{-21} level," Opt. Express **27**, 36886–36902 (2019).
35. S. Häfner, S. Herbers, S. Vogt, S. Vogt, C. Lisdat, and U. Sterr, "Transportable interrogation laser system with an instability of mod $\sigma_y = 3 \times 10^{-16}$," Opt. Express **28**, 16407–16416 (2020).
36. T. Akatsuka, T. Goh, H. Imai, K. Oguri, A. Ishizawa, I. Ushijima, N. Ohmae, M. Takamoto, H. Katori, T. Hashimoto, H. Gotoh, and T. Sogawa, "Optical frequency distribution using laser repeater stations with planar lightwave circuits," Opt. Express **28**, 9186–9197 (2020).
37. E. Cantin, M. Tønnes, R. L. Targat, A. Amy-Klein, O. Lopez, and P.-E. Pottie, "An accurate and robust metrological network for coherent optical frequency dissemination," New J. Phys. **23**, 053027 (2021).
38. G. Grosche, "Eavesdropping time and frequency: phase noise cancellation along a time-varying path, such as an optical fiber," Opt. Lett. **39**, 2545–2548 (2014).
39. C. E. Calosso, E. Bertacco, D. Calonico, C. Clivati, G. A. Costanzo, M. Frittelli, F. Levi, A. Mura, and A. Godone, "Frequency transfer via a two-way optical phase comparison on a multiplexed fiber network," Opt. Lett. **39**, 1177–1180 (2014).
40. F. Guillou-Camargo, V. Ménoret, E. Cantin, O. Lopez, N. Quintin, E. Camisard, V. Salmon, J.-M. L. Merdy, G. Santarelli, A. Amy-Klein, P.-E. Pottie, B. Desruelle, and C. Chardonnet, "First industrial-grade coherent fiber link for optical frequency standard dissemination," Appl. Opt. **57**, 7203–7210 (2018).
41. S. Droste, "Optical frequency transfer via telecommunication fiber links for metrological applications," Ph.D. thesis (Gottfried Wilhelm Leibniz Universität Hannover, 2014).
42. H. Jiang, F. Kéfélian, S. Crane, O. Lopez, M. Lours, J. Millo, D. Holleville, P. Lemonde, C. Chardonnet, A. Amy-Klein, and G. Santarelli, "Long-distance frequency transfer over an urban fiber link using optical phase stabilization," J. Opt. Soc. Am. B **25**, 2029–2035 (2008).
43. C. Clivati, P. Savio, S. Abrate, V. Curri, R. Gaudino, M. Pizzocaro, and D. Calonico, "Robust optical frequency dissemination with a dual-polarization coherent receiver," Opt. Express **28**, 8494–8511 (2020).
44. M. Notcutt, L.-S. Ma, J. Ye, and J. L. Hall, "Simple and compact 1-Hz laser system via an improved mounting configuration of a reference cavity," Opt. Lett. **30**, 1815–1817 (2005).
45. F. T. Ghaemi, "Ultra-high-precision alignment of the elastomerically mounted elements of the science camera lenses for the Mars Science Laboratory (MSL) rover," Appl. Opt. **50**, 5108–5114 (2011).
46. S. T. Dawkins, J. J. McFerran, and A. N. Luiten, "Considerations on the measurement of the stability of oscillators with frequency counters," IEEE Trans. Ultrason. Ferroelectr. Freq. Control **54**, 918–925 (2007).
47. E. Benkler, C. Lisdat, and U. Sterr, "On the relation between uncertainties of weighted frequency averages and the various types of Allan deviations," Metrologia **52**, 565 (2015).
48. R. Noe, H. Heidrich, and D. Hoffmann, "Endless polarization control systems for coherent optics," J. Lightwave Technol. **6**, 1199–1208 (1988).
49. W. Aarts and G.-D. Khoe, "New endless polarization control method using three fiber squeezers," J. Lightwave Technol. **7**, 1033–1043 (1989).
50. Schott, "Schott optical glass collection datasheets," 2019, https://www.schott.com/en-us/products/optical-glass-p1000267/downloads.
51. G. Ghosh, "Model for the pressure-optic coefficients in optical materials," Phys. Rev. B **57**, 8178–8180 (1998).

52. Corning, "Corning HPFS 7979, 7980, 8655 fused silica–optical materials product information," 2015, https://www.corning.com/media/worldwide/csm/documents/HPFS_Product_Brochure_All_Grades_2015_07_21.pdf.
53. Thorlabs, "Guide to optical glass used at Thorlabs," 2023, https://www.thorlabs.com/newgrouppage9.cfm?objectgroup_id=6973.
54. G. Ghosh, *Handbook of Thermo-Optic Coefficients of Optical Materials with Applications* (Academic, 1998).
55. P. E. Ciddor, "Refractive index of air: new equations for the visible and near infrared," Appl. Opt. **35**, 1566–1573 (1996).
56. M. Polyanskiy, 2017, https://github.com/polyanskiy/refractiveindex.info-scripts/blob/6e7febc6ea8ca76936cdfa23208f74321f018938/scripts/Ciddor 1996-air.py.
57. B. Edlén, "The refractive index of air," Metrologia **2**, 71 (1966).
58. K. P. Birch and M. J. Downs, "Correction to the updated Edlén equation for the refractive index of air," Metrologia **31**, 315–316 (1994).
59. A. Tourigny-Plante, V. Michaud-Belleau, N. B. Hébert, H. Bergeron, J. Genest, and J.-D. Deschênes, "An open and flexible digital phase-locked loop for optical metrology," Rev. Sci. Instrum. **89**, 093103 (2018).
60. G. Wanner, G. Heinzel, E. Kochkina, C. Mahrdt, B. S. Sheard, S. Schuster, and K. Danzmann, "Methods for simulating the readout of lengths and angles in laser interferometers with Gaussian beams," Opt. Commun. **285**, 4831–4839 (2012).
61. K.-S. Isleif, L. Bischof, S. Ast, D. Penkert, T. S. Schwarze, G. F. Barranco, M. Zwetz, S. Veith, J.-S. Hennig, M. Tröbs, J. Reiche, O. Gerberding, K. Danzmann, and G. Heinzel, "Towards the LISA backlink: experiment design for comparing optical phase reference distribution systems," Classical Quantum Gravity **35**, 085009 (2018).
62. K.-S. Isleif, "Laser interferometry for LISA and satellite geodesy missions," Ph.D. thesis (Gottfried Wilhelm Leibniz Universität Hannover, 2018).
63. R. Fleddermann, C. Diekmann, F. Steier, M. Tröbs, G. Heinzel, and K. Danzmann, "Sub-pm$\sqrt{\text{hz}}^{-1}$ non-reciprocal noise in the LISA backlink fiber," Classical Quantum Gravity **35**, 075007 (2018).
64. J. W. Berthold and S. F. Jacobs, "Ultraprecise thermal expansion measurements of seven low expansion materials," Appl. Opt. **15**, 2344–2347 (1976).
65. https://doi.org/10.5281/zenodo.7859474.